JACS
JOURNAL OF THE AMERICAN CHEMICAL SOCIETY
pubs.acs.org/JACS
Article

Chemically Stable Polyarylether-Based Metallophthalocyanine Frameworks with High Carrier Mobilities for Capacitive Energy Storage

Chongqing Yang, Kaiyue Jiang, Qi Zheng, Xinle Li, Haiyan Mao, Wenkai Zhong, Cheng Chen, Bing Sun, Haimei Zheng, Xiaodong Zhuang, Jeffrey A. Reimer, Yi Liu, and Jian Zhang*

Cite This: J. Am. Chem. Soc. 2021, 143, 17701−17707

Read Online

ACCESS | Metrics & More | Article Recommendations | Supporting Information

ABSTRACT: Covalent organic frameworks (COFs) with efficient charge transport and exceptional chemical stability are emerging as an import class of semiconducting materials for opto-/electronic devices and energy-related applications. However, the limited synthetic chemistry to access such materials and the lack of mechanistic understanding of carrier mobility greatly hinder their practical applications. Herein, we report the synthesis of three chemically stable polyarylether-based metallophthalocyanine COFs (PAE-PcM, M = Cu, Ni, and Co) and facile in situ growth of their thin films on various substrates (i.e., SiO_2/Si, ITO, quartz) under solvothermal conditions. We show that PAE-PcM COFs thin films with van der Waals layered structures exhibit *p*-type semiconducting properties with the intrinsic mobility up to ∼19.4 $cm^2\ V^{-1}\ s^{-1}$ and 4 orders of magnitude of increase in conductivity for PAE-PcCu film (0.2 S m^{-1}) after iodine doping. Density functional theory calculations reveal that the carrier transport in the framework is anisotropic, with the out-of-plane hole transport along columnar stacked phthalocyanine more favorable. Furthermore, PAE-PcCo shows the redox behavior maximumly contributes ∼88.5% of its capacitance performance, giving rise to a high surface area normalized capacitance of ∼19 $\mu F\ cm^{-2}$. Overall, this work not only offers fundamental understandings of electronic properties of polyarylether-based 2D COFs but also paves the way for their energy-related applications.

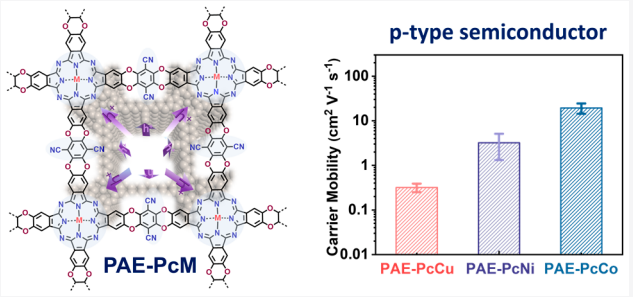

INTRODUCTION

Covalent organic frameworks (COFs) with inherent chemical tunability, ordered supramolecular lattices, and tailorable nanoporosity[1,2] have emerged as a unique class of functional crystalline materials, finding applications in gas/chemical storage and separation,[3,4] drug delivery,[5,6] chemo-sensing,[7] catalysis,[8−10] etc. In recent years, high charge carrier mobility has also been successfully realized in a number of two-dimensional (2D) COFs which exhibit outstanding (opto)-electronic properties.[11−13] In order to broaden their real applications in memory devices,[14,15] photo-/electrocatalyses,[16−19] chemiresistors,[20,21] energy storage,[22,23] among others, imparting chemical robustness in these 2D COFs is of imperative importance.[24] Synthetic chemistry to construct robust 2D COFs with high charge carrier mobility is limited, with only a few reported examples using pyrazine[20,25,26] or olefin[27] as the linkages. Recently, a new class of chemically stable 2D COFs based on the polyarylether (or dioxin) linkage was reported.[28−31] The fully planar polyarylether linkage is able to facilitate the AA-orientated stacking of planar building blocks such as triphenylene[28,29] and phthalocyanine.[30,31] It is expected that the π-stacking in these robust frameworks would facilitate numerous low-barrier carrier pathways; however, the impact of the weakened in-plane conjugation at the polyarylether linkage on the overall carrier-transporting performance is unknown. Thus, a thorough understanding of intrinsic carrier transporting behavior in these polyarylether-linked COFs is warranted.

On the other hand, besides the chemical structure, the physical form of 2D COFs also plays an important role in evaluating their carrier mobilities.[32−35] Compared with bulk powders, continuous, oriented COF thin films could potentially reduce the interference of grain boundary resistance on their intrinsic (opto)electronic properties.[12] In the past few years, the preparation of free-standing and polycrystalline COF thin films has been made possible, including air−liquid[36] and liquid−liquid[37,38] interfacial synthesis, to name a few. However, many device fabrications to evaluate COF thin

Received: August 7, 2021
Published: October 7, 2021

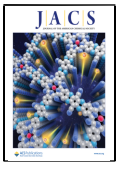

https://doi.org/10.1021/jacs.1c08265
J. Am. Chem. Soc. 2021, 143, 17701−17707

films' mobilities require harsh processing procedures, such as metal electrode deposition at high vacuum/temperature and wet-chemistry mask etching.[39] These complicated operations can sometimes lead to cracking or even exfoliation of the thin films from substrates.[40,41] Therefore, improving the compatibility of COF thin films with applicable substrates while retaining their crystallinity remains a crucial task.

Herein, we report the synthesis of three chemically stable polyarylether-based metallophthalocyanine (PAE-PcM) COFs and the facile in situ growth of their thin films on various substrates (i.e., SiO_2/Si, ITO, quartz) under solvothermal conditions. Despite the weakened in-plane π-conjugation, the PAE-PcM COF thin films with van der Waals layered structures exhibit p-type semiconducting properties with high mobilities up to 19.4 $cm^2 V^{-1} s^{-1}$. The intrinsic conductivity of 3.8×10^{-5} S m^{-1} for the PAE-PcCu film can increase by 4 orders of magnitude to 0.2 S m^{-1} after iodine doping. DFT calculations reveal that the columnar stacking of phthalocyanine macrocycles mostly contributes to the overall carrier-transporting properties and consequently the exceedingly small bandgaps. Furthermore, capacitance studies showed that rich redox sites in chemically stable PAE-PcCo maximumly contributed to 88.5% of its energy storage performance, yielding a high surface area normalized capacitance of ~19 μF cm^{-2} and a good long-term durability. Our work not only provides a thorough understanding of electronic properties of polyarylether-based 2D COFs but also paves the way for exploring structurally controllable materials toward practical electrochemical energy-storage applications.

RESULTS AND DISCUSSION

Synthesis and Characterization of Bulk PAE-PcM. The three PAE-PcM COFs (M = Cu, Ni, and Co) were constructed through the nucleophilic aromatic substitution reactions (S_NAr) of (2,3,9,10,16,17,23,24-octahydroxylphthalocyaninato)metal(II) ($PcMOH_8$) and tetrafluoroterephthalonitrile (TFPN) (Figure 1a; experimental details in the Supporting Information). Their crystal structure was first characterized by the wide-angle X-ray scattering (WAXS) in combination with density functional theory (DFT) calculations. As shown in Figure 1b, the strong distinct diffraction peaks at 4.57°, 9.39°, and 27.15° for PAE-PcCu can be assigned to the (100), (200), and (001) facets, respectively (Figure 1b), indicating a lamella tetragonal framework. Simulated diffraction peaks of the eclipsed AA stacked structure ($a = b = 20.19$ Å, $c = 3.59$ Å, $\alpha = \beta = \gamma = 90°$) are in good agreement with experimental diffraction peaks (Figures 1b and S1–3). In addition, the broad peak at 27.15° corresponds to the (001) facet with an interlayer distance of ~3.3 Å. PAE-PcNi and PAE-PcCo also exhibit similar tetragonal layered structures in the eclipsed AA stacking mode (Figure S4). According to the Scherrer equation, the average crystallinities from WAXS analysis were estimated to be ~57, ~62, and ~28 nm, respectively. High-resolution transmission electron microscopy (HRTEM) of PAE-PcCu and its corresponding fast Fourier transform (FFT) analysis further evidence the square lattices with $a = b =$ ~2 nm, which are in good consistence with the WAXS analysis (Figures 1c and S5). The corresponding elemental mappings demonstrate the aggregated particles in as-made powders and the homogeneous distribution of carbon, nitrogen, oxygen, and metal elements throughout the frameworks (Figures S6–S8).

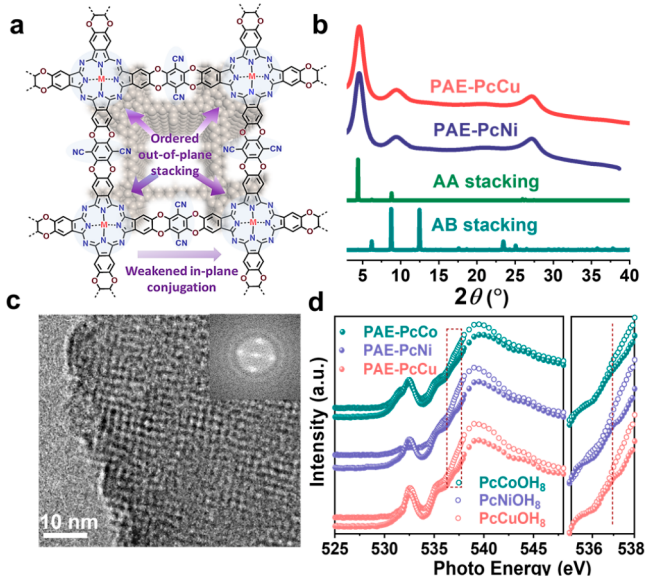

Figure 1. (a) Schematic illustration of PAE-PcM (M = Cu, Ni and Co) with weakened in-plane conjugation and ordered out-of-plane stacking. (b) Experimental WAXS pattern for PAE-PcCu (red) and PAE-PcNi (purple) and simulations based on eclipsed AA (green) and AB (dark cyan) stacking (λ = 1.54 Å). (c) High-resolution TEM images of PAE-PcCu. Inset: corresponding fast Fourier transform (FFT) result. (d) Oxygen K-edge XANES spectra for PAE-PcM and $PcMOH_8$.

The successful formation of ether bond was confirmed by the new peaks centered at ~1260 and ~1040 cm^{-1} for PAE-PcM COFs in the Fourier-transform infrared (FTIR) spectra (Figure S9).[29] To further probe the chemical environment of oxygen, *K*-edge X-ray absorption near-edge spectroscopy (XANES) was employed (Figure 1d), and a new feature around 536.9 eV can be assigned to the transitions from the 1s electron of the central oxygen to the 2pπ* (O 1s-π*; C−O−C).[42,43] In addition, the broad peak centered at 544 eV corresponds with the O 1s-σ* (C−O) excitation.[44] X-ray photoelectron spectroscopy (XPS) also revealed the presence of C, N, O, and metal atoms as well as a trace amount of F (Figures S10–12). From the content of residue F, the conversions of the S_NAr reaction were calculated as 75.6%, 84.5%, and 74.8% for PAE-PcCu, -PcNi, and -PcCo, respectively.[29] Deconvolution of the O(1s) signal for PAE-PcCu generates two peaks centered at 532.7 and 533.8 eV, which can be attributed to the aromatic C−O−C bond and adsorbed H_2O/CO_2 from the atmosphere (Figures S13).[45] The core-level spectrum of Cu(2p) resembled that of $PcCuOH_8$ with two dominant peaks at 940.0 eV (Cu $2p_{3/2}$) and 954.9 eV (Cu $2p_{1/2}$), which indicates the presence of Cu(II) in the tetragonal framework (Figure S14). Analogous results from deconvolution of O(1s) and transition metal atoms (2p) were obtained for PAE-PcNi and PAE-PcCo (Figures S15 and S16), respectively.

The porosity of PAE-PcM was further measured by nitrogen sorption at 77 K, and all isotherms show sharp uptakes at the low-pressure range ($P/P_0 < 0.05$), indicating the microporous nature for the frameworks (Figure S17). The Brunauer−Emmett−Teller surface areas (SA_{BET}) were calculated to be 402, 363, and 308 $m^2 g^{-1}$ for PAE-PcCu, -PcNi, and -PcCo, respectively. The related pore size distribution demonstrates an average pore size of ~1.4 nm (Figure S18 and Table S1). Due

https://doi.org/10.1021/jacs.1c08265
J. Am. Chem. Soc. 2021, 143, 17701−17707

to the ultrastable polyarylether linkages, the obtained COFs showed great chemical robustness. No apparent loss of crystallinity was observed after the treatment under harsh conditions such as polar solvent in NMP (*N*-methyl-2-pyrrolidone), boiling water, concentrated HCl (12 M), and KOH (7 and 14 M) solutions (Figures S19 and S20).

Theoretical Electronic Structures of PAE-PcM. Owing to the small distance (~3.3 Å) between the close-packed phthalocyanine rings, it is believed that considerable carrier transport could occur in PAE-PcM COFs. DFT calculations were first employed to study the intrinsic electronic band structures of PAE-PcM COFs (details in the experimental section of the Supporting Information). The electronic band structure and the projected density of states (PDOS) for monolayer and multilayer models of PAE-PcCu were first calculated (Figures 2a–c), and the band structure of the

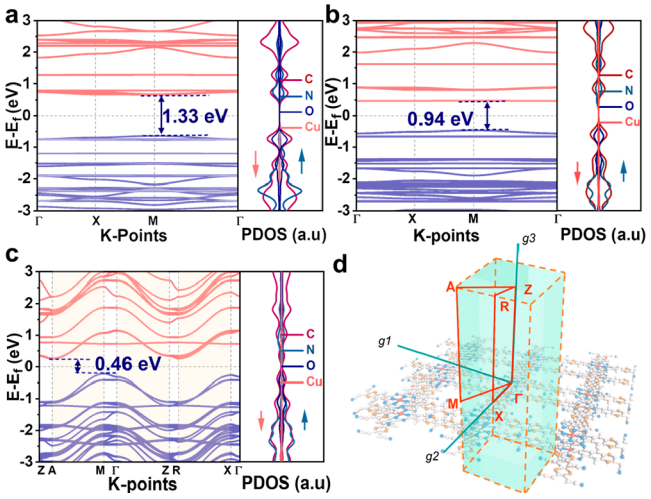

Figure 2. (a) Calculated band structure of a monolayer PAE-PcCu with GGA+U correction and the corresponding projected density of states (PDOS) for C (p), N(p), O(p), and Cu(d) states (red arrow: spin-down; blue arrow: spin-up). (b) Electronic band structure of eclipsed AA stacked PAE-PcCu multilayers along the in-plane high symmetry K-points. (c) Calculated band structure of PAE-PcCu multilayers along in-plane and out-of-plane high symmetry K-points. The light-yellow regions are pathways along the out-of-plane directions. (d) Corresponding first Brillouin zone and high symmetry K-points.

monolayer shows the typical semiconducting feature with a direct bandgap of ~1.33 eV. The relatively flat conduction band (CB) and valence band (VB) indicate that the charge transport along the 2D plane is relatively null due to the localized electron density trapped within the phthalocyanine moiety. Notably, the stacked multilayer structure along in-plane direction (Γ-X and M-Γ; Figure 2b,d) showed slightly improved band dispersion with a moderate bandgap of ~0.94 eV. In contrast, the band structures along all high symmetry *K*-points (Z-A, M-Γ, Z-R, and X-Γ; Figure 2c,d) demonstrated a distinctly reduced bandgap of 0.46 eV with appreciable band dispersion. These results indicate that the charge transport in multilayered PAE-PcCu is anisotropic and the pathways from interlayer $\pi-\pi$ interactions are much more favorable to the carrier mobility due to the formation of periodic π-columns.[20,46] The average carrier effective mass along the out-of-plane direction was calculated to be $m_h = 1.2m_0$* and $m_e = 1.5m_0$* for holes and electrons, respectively, further suggesting that the hole mobility in the out-of-plane direction is more favorable. PAE-PcNi and PAE-PcCo multilayer models also demonstrate similar indirect bandgaps of 0.52 and 0.51 eV, respectively (Figures S21 and 22). Taken together, the DFT calculation reveals that the metal center has a neglectable effect on the electronic band-structures on PAE-PcM COFs.[25]

Film Preparation and Characterization. Next, the charge transport behavior of PAE-PcM frameworks was analyzed experimentally. In consideration of the challenges posed by the numerous grain boundaries of bulk COF powders, the direct growth of oriented thin films of PAE-PcM on confined interfaces was explored to reveal their intrinsic electronic properties. The PAE-PcM films were prepared on ITO, quartz, and Si/SiO_2 substrates via solvothermal reactions (Figure 3a and Figure S23; see the

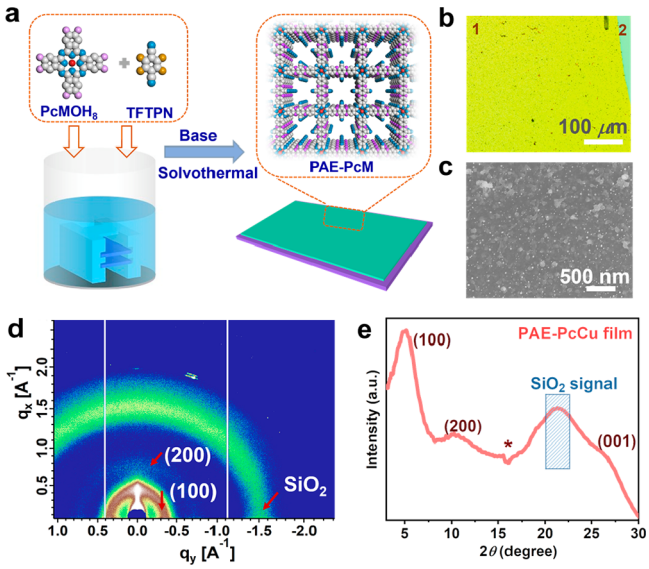

Figure 3. (a) Schematic illustration of in situ growth of PAE-PcM films on different substrates via solvothermal reactions. (b) Optical microscope image of PAE-PcCu and (c) the corresponding SEM image, indicating a homogeneous and continuous film. (d) The GIWAXS pattern of PAE-PcCu film grown on a SiO_2/Si substrate. (e) Corresponding 1D diffraction pattern converted from circular integration average of GIWAXS result (λ = 1.54 Å). Dotted frames indicate the SiO_2 signals from the substrate. Asterisk is the artifact.

Supporting Information for a detailed synthesis procedure). Their morphologies were characterized by optical microscopy (OM), scanning electron microscopy (SEM), and atomic force microscopy (AFM). The OM and SEM images demonstrated that all films are continuous with a microscopic lateral size of several millimeters (Figure 3b,c and Figure S24). Tapping mode AFM was then used to characterize the obtained thin films, and based on the cross-sectional analysis, the average thicknesses of PAE-PcCu, PcNi, and PcCo are 46, 86, and 78 nm, respectively (Figure S25). The grazing-incidence wide-angle X-ray scattering (GIWAXS) studies further confirmed the formation of crystalline COF thin films. As shown in Figure 3d,e, the corresponding GIWAXS patterns for a PAE-PcCu thin film showed strong reflections at ~0.42, 0.75, and 1.60 $Å^{-1}$ with the corresponding d-spacings of 18.4, 9.0, and 3.5 Å, respectively, indicating the successful formation of layered tetragonal lattices of PAE-PcCu with an interlayer d-spacing of 3.5 Å on the confined interfaces, consistent with the WAXS result of the bulk powder sample. Similar results were obtained

https://doi.org/10.1021/jacs.1c08265
J. Am. Chem. Soc. 2021, 143, 17701−17707

for PAE-PcNi and PAE-PcCo films. Corresponding average crystallinity from GIWAXS analysis were estimated to be ~24, ~40, and ~105 nm, respectively (Figures S26 and S27).

Opto-/Electronic Properties and Mobilities in PAE-PcM films. The optoelectronic properties of the PAE-PcM films were then evaluated by UV/vis spectroscopy and cyclic voltammetry (CV). As shown in Figure S28, the typical Q-band (~700 nm) and Soret band (~416 nm) were observed for all three films (on quartz). The corresponding indirect optical bandgaps were calculated to be 1.27, 1.42, and 1.50 eV for PAE-PcCo, -PcNi, and -PcCu, respectively (Figure 4a).

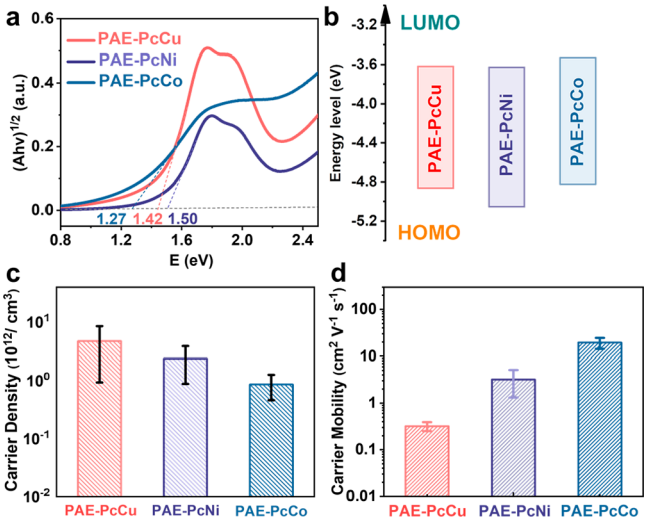

Figure 4. (a) Tauc plots of PAE-PcM thin films. (b) Experimental HOMO and LUMO energy levels of PAE-PcM calculated from CV. (c) Average carrier density and (d) carrier mobility of PAE-PcM thin films obtained from Hall effect measurements.

Electrochemical bandgaps from CV measurements show similar values for PAE-PcCo (1.29 eV), PAE-PcNi (1.40 eV), and PAE-PcCu (1.22 eV), as shown in Figures 4b and S29. To evaluate their carrier mobilities, Hall effect measurements were conducted at room temperature after depositing four gold electrodes on top of the COF films on Si/SiO_2 (Experimental Section; Figure S30). The results reveal that all PAE-PcM COFs are *p*-type semiconductors with inferred average charge carrier densities of $4.7(\pm3.8) \times 10^{12}$, $2.4(\pm1.5) \times 10^{12}$, and $0.7(\pm0.4) \times 10^{12}$ cm^{-3} for PAE-PcCu, -PcNi and -PcCo, respectively (Figure 4c and Table S2). The corresponding Hall mobility in the *dc* limit shows that PAE-PcCo has the highest carrier mobilities of ~19.4 (±5.1) cm^2 V^{-1} s^{-1}, while the carrier mobilities of PAE-PcNi and PAE-PcCu are $3.2(\pm1.9)$ and $3.0(\pm0.7) \times 10^{-1}$ cm^2 V^{-1} s^{-1}, respectively (Figure S31). These results show that the tetragonal framework with the cobalt center exhibits the best transport performance that ranks among state-of-art COF semiconductors (Table S3). Notably, the difference in mobility among the three PAE-PcM COFs could be attributed to the intrinsic different scattering of the metal centers and some extrinsic factors such as grain boundary diffraction, crystalline domain orientation, etc.[25] Besides, the conductivities generated from Hall effect measurements were $2.6(\pm2.3) \times 10^{-5}$, $9.3(\pm0.6) \times 10^{-5}$ and $1.9(\pm0.5) \times 10^{-4}$ S m^{-1}, respectively (Figure 4d and Table S2). We also measured the electrical dc conductivity of the as-made PAE-PcCu film via a two-probe method and observed a linear current−voltage (*I*−*V*) relationship, and a conductivity of $\sim3.8 \times 10^{-5}$ S m^{-1}, similar to the results from Hall effect results (Figures 4d, S32, and S33). This value is comparable with previously reported phthalocyanine-based COFs such as CuPc-pz[25] (3.3×10^{-5} S m^{-1}) and NiPc-CoTAA[21] (8.2×10^{-3} S m^{-1}). Notably, after iodine doping,[20] a 4 orders of magnitude increase of the conductivity could be observed, reaching 0.2 S m^{-1} (Table S4).

Electrochemical Performance of PAE-PcCo electrode. Considering its good porosity, carrier transport property, and high chemical stability, the capacitance behavior of PAE-PcCo was further explored. Owing to its large open channels of ~1.4 nm, PAE-PcCo could accommodate large electrolyte ions, e.g., 1-ethyl-3-methyl-imidazolium ($EMIm^+$; size 0.8 nm[47]). A 3-electrode system in 0.5 M [EMIm]Cl electrolyte was used to study the electrochemical performance (experimental section in the Supporting Information). As shown in Figure S33, CV curves of PAE-PcCo showed stable potential windows both cycled catholically (−0.6−0.0 V) and anodically (0.0−0.8 V) with three pairs of broad redox peaks at −0.2, 0.2, and 0.4 V, suggesting the capacitance characteristics of PAE-PcCo in a wide potential window range of −0.6−0.8 V, with charge storage contribution from both electrical double-layer capacitance (diffusion-controlled, C_{dl}) and pseudocapacitance (redox process, C_p). The detailed capacitance contributions of C_{dl} and C_p were then subsequentially studied via the Dunn method[48] using a quasi-solid-state symmetric supercapacitor with [EMImCl]/acetonitrile (0.5 M) as the electrolyte. In the working voltage window of 0−1.4 V, the CV curves at different scan rates showed similar rectangular shapes with quite broad redox peaks (Figure S34). The relationship between the current and scan rate was first studied at low scan rates, and the corresponding *b*-values at different potentials were calculated to be 0.64, 0.61, 0.61, 0.65, 0.69, 0.75, and 0.85 at 0.4, 0.6, 0.8, 1.0, 1.1, 1.2, and 1.3 V, respectively (Figure S35). Since a *b*-value of 1.0 represents an ideal pseudocapacitive process from redox reactions, while a *b*-value of 0.5 means a diffusion-controlled process,[49] our results strongly indicate that the charge storage behavior of PAE-PcCo is contributed from both diffusion-controlled (C_{dl}) and capacitive redox process (C_p). As shown in Figure 5a, the C_p contributes a smaller fraction (~33.3%) of total capacitance behavior at 2 mV s^{-1}. As the scan rate increases, the contribution of C_p increases up to 88.7% at a scan rate of 80 mV s^{-1} (Figure 5b). Moreover, the capacitive differentiation from Trasatti analysis[50] also indicates that the maximum redox contribution is ~88.5%, which is in excellent agreement with that from Dunn analysis (Figure S36). All these results confirmed that the Faradaic reactions of redox-active sites in PAE-PcCo showed a dominant contribution to the total capacitive behavior at high scan speed.

According to the CV curves, the corresponding normalized capacitance to specific surface area of PAE-PcCo is 19 μF cm^{-2} (Figure S37), apparently higher than several other pure electric double-layer capacitor materials and porous frameworks (Figure S38), such as active graphene (5 μF cm^{-2}; SA_{BET} = 3523 cm^2 g^{-1}),[51] single-walled CNTs (12 μF cm^{-2}; SA_{BET} = 1300 cm^2 g^{-1}),[52] and chemically reduced graphene (7 μF cm^{-2}; SA_{BET} = 2400 cm^2 g^{-1}).[53] This result further confirmed that the capacitance of PAE-PcCo is mostly attributed to its redox behavior during the energy storage process, with a minor contribution from the double-layer capacitance. Owing to the robust chemical stability of PAE-PcCo, the device also showed good stability, with 86% maintenance after 1500 cycles at 80 mV s^{-1} (Figures 5c and S39). The EIS profile for the solid-

https://doi.org/10.1021/jacs.1c08265
J. Am. Chem. Soc. 2021, 143, 17701−17707

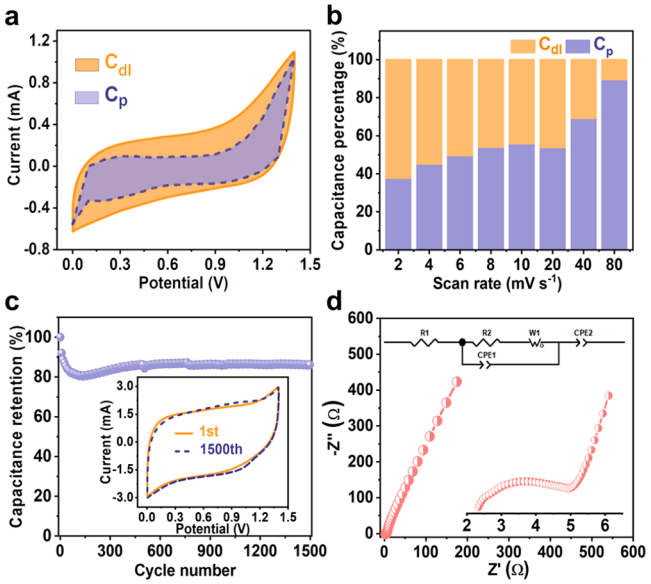

Figure 5. (a) Respective capacitance contribution of PAE-PcCo at scan rate of 2 mV s^{-1}. (b) Percentage of capacitance contribution at different scan rates. (c) Cycling stability test at 80 mV s^{-1}. Inset: comparison of initial and 1500th CV curve. (d) Nyquist plot. Inset: equivalent circuit of PAE-PcCo electrode (R1: solution resistance; R2: charge transfer resistance; W: Warburg impedance).

state supercapacitor cell exhibits an almost vertical low-frequency region in the Nyquist plot with a low equivalent Ohmic resistance of 2.2 Ω (Figure 5d), which verifies a superior accessibility of ions to active sites. Thanks to the low internal resistance, intrinsic porosity, and rich redox behavior of electrode materials, the PAE-PcCo based device delivered a high capacitance.

CONCLUSION

In summary, we have synthesized a series of layered polyarylether-based metallophthalocyanine frameworks. These PAE-PcM COFs demonstrate robust chemical stability and intrinsic p-type semiconducting behavior with high carrier mobility up to ∼19.4 cm^2 V^{-1} s^{-1}, and the intrinsic conductivity of PAE-PcCu film can increase by 4 orders of magnitude to 0.2 S m^{-1} after iodine doping. As a proof-of-concept application, the high mobility PAE-PcCo COF was used as an electrode material for all-solid-state supercapacitors. The capacitance was found to be mostly attributable to the redox process during charge−discharge cycles, with a maximum contribution of 88.5%. The device exhibits a high surface area normalized capacitance of ∼19 μF cm^{-2} and a good long-term capacitance retention of 86% after 1500 cycles. The combined experimental and theoretical studies provide fundamental understandings of the electronic properties of polyarylether-based 2D COFs, which paves the way for their future energy-related applications.

ASSOCIATED CONTENT

Supporting Information

The Supporting Information is available free of charge at https://pubs.acs.org/doi/10.1021/jacs.1c08265.

Synthesis and structural characterization of PAE-PcM and thin films; DFT calculations; electrochemical measurements (PDF)

AUTHOR INFORMATION

Corresponding Author

Jian Zhang − *The Molecular Foundry, Lawrence Berkeley National Laboratory, Berkeley, California 94720, United States;* orcid.org/0000-0003-0274-0814; Email: jianzhang@lbl.gov

Authors

Chongqing Yang − *The Molecular Foundry, Lawrence Berkeley National Laboratory, Berkeley, California 94720, United States*

Kaiyue Jiang − *The meso-Entropy Matter Lab, School of Chemistry and Chemical Engineering, Shanghai Jiao Tong University, Shanghai 200240, China*

Qi Zheng − *Materials Sciences Division, Lawrence Berkeley National Laboratory, Berkeley, California 94720, United States*

Xinle Li − *The Molecular Foundry, Lawrence Berkeley National Laboratory, Berkeley, California 94720, United States; Materials Sciences Division, Lawrence Berkeley National Laboratory, Berkeley, California 94720, United States; Department of Chemistry, Clark Atlanta University, Atlanta, Georgia 30314, United States*

Haiyan Mao − *Department of Chemical and Biomolecular Engineering, University of California, Berkeley, California 94720, United States*

Wenkai Zhong − *Advanced Light Source, Lawrence Berkeley National Laboratory, Berkeley, California 94720, United States; Frontiers Science Center for Transformative Molecules, In-situ Center for Physical Science, and Center of Hydrogen Science, School of Chemistry and Chemical Engineering, Shanghai Jiao Tong University, Shanghai 200240, China;* orcid.org/0000-0001-8333-4898

Cheng Chen − *The meso-Entropy Matter Lab, School of Chemistry and Chemical Engineering, Shanghai Jiao Tong University, Shanghai 200240, China*

Bing Sun − *The Molecular Foundry, Lawrence Berkeley National Laboratory, Berkeley, California 94720, United States; School of Science, China University of Geosciences (Beijing), Beijing 100083, China;* orcid.org/0000-0001-5917-3094

Haimei Zheng − *Materials Sciences Division, Lawrence Berkeley National Laboratory, Berkeley, California 94720, United States;* orcid.org/0000-0003-3813-4170

Xiaodong Zhuang − *The meso-Entropy Matter Lab, School of Chemistry and Chemical Engineering, Shanghai Jiao Tong University, Shanghai 200240, China;* orcid.org/0000-0001-7685-5142

Jeffrey A. Reimer − *Materials Sciences Division, Lawrence Berkeley National Laboratory, Berkeley, California 94720, United States; Department of Chemical and Biomolecular Engineering, University of California, Berkeley, California 94720, United States;* orcid.org/0000-0002-4191-3725

Yi Liu − *The Molecular Foundry, Lawrence Berkeley National Laboratory, Berkeley, California 94720, United States; Materials Sciences Division, Lawrence Berkeley National Laboratory, Berkeley, California 94720, United States;* orcid.org/0000-0002-3954-6102

Complete contact information is available at: https://pubs.acs.org/10.1021/jacs.1c08265

Notes

The authors declare no competing financial interest.

https://doi.org/10.1021/jacs.1c08265
J. Am. Chem. Soc. 2021, 143, 17701−17707

■ ACKNOWLEDGMENTS

Work at the Molecular Foundry and Advanced Light Source was supported by the Office of Science, Office of Basic Energy Sciences, of the U.S. Department of Energy, and by the Laboratory Directed Research and Development Program of Lawrence Berkeley National Laboratory under U.S. Department of Energy contract no. DE-AC02-05CH11231. K.J., C.C., and X.Z acknowledge the financial support from NSFC (51973114, 21720102002). J.A.R. acknowledges support from the Department of Energy (DOE), Office of Basic Energy Sciences, Division of Materials Sciences and Engineering (contract no. DE-AC02-76SF00515). X.L. and Y.L. acknowledge the support from the U.S. Department of Energy, Office of Science, Office of Basic Energy Sciences, Materials Sciences and Engineering Division, under contract no. DE-AC02-05CH11231 within the Inorganic/Organic Nanocomposites Program (KC3104). H.Z. acknowledges the support of the U.S. Department of Energy, Office of Science, Office of Basic Energy Sciences, Materials Sciences and Engineering Division under Contract No. DE-AC02-05-CH11231 within the KC22ZH program.

■ REFERENCES

(1) Diercks, C. S.; Yaghi, O. M. The atom, the molecule, and the covalent organic framework. *Science* **2017**, *355* (6328), eaal1585.
(2) Geng, K.; He, T.; Liu, R.; Dalapati, S.; Tan, K. T.; Li, Z.; Tao, S.; Gong, Y.; Jiang, Q.; Jiang, D. Covalent Organic Frameworks: Design, Synthesis, and Functions. *Chem. Rev.* **2020**, *120* (16), 8814−8933.
(3) Huang, N.; Chen, X.; Krishna, R.; Jiang, D. Two-dimensional covalent organic frameworks for carbon dioxide capture through channel-wall functionalization. *Angew. Chem., Int. Ed.* **2015**, *54* (10), 2986−2990.
(4) Ma, Y. X.; Li, Z. J.; Wei, L.; Ding, S. Y.; Zhang, Y. B.; Wang, W. A Dynamic Three-Dimensional Covalent Organic Framework. *J. Am. Chem. Soc.* **2017**, *139* (14), 4995−4998.
(5) Fang, Q.; Wang, J.; Gu, S.; Kaspar, R. B.; Zhuang, Z.; Zheng, J.; Guo, H.; Qiu, S.; Yan, Y. 3D Porous Crystalline Polyimide Covalent Organic Frameworks for Drug Delivery. *J. Am. Chem. Soc.* **2015**, *137* (26), 8352−8355.
(6) Mitra, S.; Sasmal, H. S.; Kundu, T.; Kandambeth, S.; Illath, K.; Diaz Diaz, D.; Banerjee, R. Targeted Drug Delivery in Covalent Organic Nanosheets (CONs) via Sequential Postsynthetic Modification. *J. Am. Chem. Soc.* **2017**, *139* (12), 4513−4520.
(7) Wu, X.; Han, X.; Xu, Q.; Liu, Y.; Yuan, C.; Yang, S.; Liu, Y.; Jiang, J.; Cui, Y. Chiral BINOL-Based Covalent Organic Frameworks for Enantioselective Sensing. *J. Am. Chem. Soc.* **2019**, *141* (17), 7081−7089.
(8) Lu, S.; Hu, Y.; Wan, S.; McCaffrey, R.; Jin, Y.; Gu, H.; Zhang, W. Synthesis of Ultrafine and Highly Dispersed Metal Nanoparticles Confined in a Thioether-Containing Covalent Organic Framework and Their Catalytic Applications. *J. Am. Chem. Soc.* **2017**, *139* (47), 17082−17088.
(9) Wang, X.; Chen, L.; Chong, S. Y.; Little, M. A.; Wu, Y.; Zhu, W. H.; Clowes, R.; Yan, Y.; Zwijnenburg, M. A.; Sprick, R. S.; Cooper, A. I. Sulfone-containing covalent organic frameworks for photocatalytic hydrogen evolution from water. *Nat. Chem.* **2018**, *10* (12), 1180−1189.
(10) Bi, S.; Yang, C.; Zhang, W.; Xu, J.; Liu, L.; Wu, D.; Wang, X.; Han, Y.; Liang, Q.; Zhang, F. Two-dimensional semiconducting covalent organic frameworks via condensation at arylmethyl carbon atoms. *Nat. Commun.* **2019**, *10* (1), 2467.
(11) Allendorf, M. D.; Dong, R.; Feng, X.; Kaskel, S.; Matoga, D.; Stavila, V. Electronic Devices Using Open Framework Materials. *Chem. Rev.* **2020**, *120* (16), 8581−8640.
(12) Keller, N.; Bein, T. Optoelectronic processes in covalent organic frameworks. *Chem. Soc. Rev.* **2021**, *50* (3), 1813−1845.
(13) Cai, S.-L.; Zhang, Y.-B.; Pun, A. B.; He, B.; Yang, J.; Toma, F. M.; Sharp, I. D.; Yaghi, O. M.; Fan, J.; Zheng, S.-R.; Zhang, W.-G.; Liu, Y. Tunable electrical conductivity in oriented thin films of tetrathiafulvalene-based covalent organic framework. *Chem. Sci.* **2014**, *5* (12), 4693−4700.
(14) Park, S.; Liao, Z.; Ibarlucea, B.; Qi, H.; Lin, H. H.; Becker, D.; Melidonie, J.; Zhang, T.; Sahabudeen, H.; Baraban, L.; Baek, C. K.; Zheng, Z.; Zschech, E.; Fery, A.; Heine, T.; Kaiser, U.; Cuniberti, G.; Dong, R.; Feng, X. Two-Dimensional Boronate Ester Covalent Organic Framework Thin Films with Large Single Crystalline Domains for a Neuromorphic Memory Device. *Angew. Chem., Int. Ed.* **2020**, *59* (21), 8218−8224.
(15) Sun, B.; Li, X.; Feng, T.; Cai, S.; Chen, T.; Zhu, C.; Zhang, J.; Wang, D.; Liu, Y. Resistive Switching Memory Performance of Two-Dimensional Polyimide Covalent Organic Framework Films. *ACS Appl. Mater. Interfaces* **2020**, *12* (46), 51837−51845.
(16) Lin, S.; Diercks, C. S.; Zhang, Y. B.; Kornienko, N.; Nichols, E. M.; Zhao, Y.; Paris, A. R.; Kim, D.; Yang, P.; Yaghi, O. M.; Chang, C. J. Covalent organic frameworks comprising cobalt porphyrins for catalytic CO2 reduction in water. *Science* **2015**, *349* (6253), 1208−1213.
(17) Biswal, B. P.; Vignolo-Gonzalez, H. A.; Banerjee, T.; Grunenberg, L.; Savasci, G.; Gottschling, K.; Nuss, J.; Ochsenfeld, C.; Lotsch, B. V. Sustained Solar H2 Evolution from a Thiazolo[5,4-d]thiazole-Bridged Covalent Organic Framework and Nickel-Thiolate Cluster in Water. *J. Am. Chem. Soc.* **2019**, *141* (28), 11082−11092.
(18) Xu, S.; Sun, H.; Addicoat, M.; Biswal, B. P.; He, F.; Park, S.; Paasch, S.; Zhang, T.; Sheng, W.; Brunner, E.; Hou, Y.; Richter, M.; Feng, X. Thiophene-Bridged Donor-Acceptor sp2-Carbon-Linked 2D Conjugated Polymers as Photocathodes for Water Reduction. *Adv. Mater.* **2021**, *33* (1), 2006274.
(19) Han, B.; Ding, X.; Yu, B.; Wu, H.; Zhou, W.; Liu, W.; Wei, C.; Chen, B.; Qi, D.; Wang, H.; Wang, K.; Chen, Y.; Chen, B.; Jiang, J. Two-Dimensional Covalent Organic Frameworks with Cobalt(II)-Phthalocyanine Sites for Efficient Electrocatalytic Carbon Dioxide Reduction. *J. Am. Chem. Soc.* **2021**, *143* (18), 7104−7113.
(20) Meng, Z.; Stolz, R. M.; Mirica, K. A. Two-Dimensional Chemiresistive Covalent Organic Framework with High Intrinsic Conductivity. *J. Am. Chem. Soc.* **2019**, *141* (30), 11929−11937.
(21) Yue, Y.; Cai, P.; Xu, X.; Li, H.; Chen, H.; Zhou, H. C.; Huang, N. Conductive Metallophthalocyanine Framework Films with High Carrier Mobility as Efficient Chemiresistors. *Angew. Chem., Int. Ed.* **2021**, *60* (19), 10806−10813.
(22) Vitaku, E.; Gannett, C. N.; Carpenter, K. L.; Shen, L.; Abruna, H. D.; Dichtel, W. R. Phenazine-Based Covalent Organic Framework Cathode Materials with High Energy and Power Densities. *J. Am. Chem. Soc.* **2020**, *142* (1), 16−20.
(23) Singh, V.; Byon, H. R. Advances in electrochemical energy storage with covalent organic frameworks. *Mater. Adv.* **2021**, *2* (10), 3188−3212.
(24) Li, X.; Cai, S.; Sun, B.; Yang, C.; Zhang, J.; Liu, Y. Chemically Robust Covalent Organic Frameworks: Progress and Perspective. *Matter* **2020**, *3* (5), 1507−1540.
(25) Wang, M.; Ballabio, M.; Wang, M.; Lin, H. H.; Biswal, B. P.; Han, X.; Paasch, S.; Brunner, E.; Liu, P.; Chen, M.; Bonn, M.; Heine, T.; Zhou, S.; Canovas, E.; Dong, R.; Feng, X. Unveiling Electronic Properties in Metal-Phthalocyanine-Based Pyrazine-Linked Conjugated Two-Dimensional Covalent Organic Frameworks. *J. Am. Chem. Soc.* **2019**, *141* (42), 16810−16816.
(26) Huang, N.; Lee, K. H.; Yue, Y.; Xu, X.; Irle, S.; Jiang, Q.; Jiang, D. A Stable and Conductive Metallophthalocyanine Framework for Electrocatalytic Carbon Dioxide Reduction in Water. *Angew. Chem., Int. Ed.* **2020**, *59* (38), 16587−16593.
(27) Jin, E.; Asada, M.; Xu, Q.; Dalapati, S.; Addicoat, M. A.; Brady, M. A.; Xu, H.; Nakamura, T.; Heine, T.; Chen, Q.; Jiang, D. Two-dimensional sp2 carbon-conjugated covalent organic frameworks. *Science* **2017**, *357* (6352), 673−676.
(28) Zhang, B.; Wei, M.; Mao, H.; Pei, X.; Alshmimri, S. A.; Reimer, J. A.; Yaghi, O. M. Crystalline Dioxin-Linked Covalent Organic

Frameworks from Irreversible Reactions. *J. Am. Chem. Soc.* **2018**, *140* (40), 12715−12719.
(29) Guan, X.; Li, H.; Ma, Y.; Xue, M.; Fang, Q.; Yan, Y.; Valtchev, V.; Qiu, S. Chemically stable polyarylether-based covalent organic frameworks. *Nat. Chem.* **2019**, *11* (6), 587−594.
(30) Lu, M.; Zhang, M.; Liu, C. G.; Liu, J.; Shang, L. J.; Wang, M.; Chang, J. N.; Li, S. L.; Lan, Y. Q. Stable Dioxin-Linked Metallophthalocyanine Covalent Organic Frameworks (COFs) as Photo-Coupled Electrocatalysts for CO2 Reduction. *Angew. Chem., Int. Ed.* **2021**, *60* (9), 4864−4871.
(31) Lei, Z.; Lucas, F. W. S.; Canales Moya, E.; Huang, S.; Rong, Y.; Wesche, A.; Li, P.; Bodkin, L.; Jin, Y.; Holewinski, A.; Zhang, W. Highly stable dioxin-linked metallophthalocyanine covalent organic frameworks. *Chin. Chem. Lett.* **2021**, DOI: 10.1016/j.cclet.2021.04.047.
(32) Medina, D. D.; Petrus, M. L.; Jumabekov, A. N.; Margraf, J. T.; Weinberger, S.; Rotter, J. M.; Clark, T.; Bein, T. Directional Charge-Carrier Transport in Oriented Benzodithiophene Covalent Organic Framework Thin Films. *ACS Nano* **2017**, *11* (3), 2706−2713.
(33) Ghosh, R.; Paesani, F. Unraveling the effect of defects, domain size, and chemical doping on photophysics and charge transport in covalent organic frameworks. *Chem. Sci.* **2021**, *12* (24), 8373−8384.
(34) Castano, I.; Evans, A. M.; Reis, R. d.; Dravid, V. P.; Gianneschi, N. C.; Dichtel, W. R. Mapping Grains, Boundaries, and Defects in 2D Covalent Organic Framework Thin Films. *Chem. Mater.* **2021**, *33* (4), 1341−1352.
(35) Wang, H.; He, B.; Liu, F.; Stevens, C.; Brady, M. A.; Cai, S.; Wang, C.; Russell, T. P.; Tan, T. W.; Liu, Y. Orientation transitions during the growth of imine covalent organic framework thin films. *J. Mater. Chem. C* **2017**, *5* (21), 5090−5095.
(36) Liu, K.; Qi, H.; Dong, R.; Shivhare, R.; Addicoat, M.; Zhang, T.; Sahabudeen, H.; Heine, T.; Mannsfeld, S.; Kaiser, U.; Zheng, Z.; Feng, X. On-water surface synthesis of crystalline, few-layer two-dimensional polymers assisted by surfactant monolayers. *Nat. Chem.* **2019**, *11* (11), 994−1000.
(37) Dey, K.; Pal, M.; Rout, K. C.; Kunjattu, H. S.; Das, A.; Mukherjee, R.; Kharul, U. K.; Banerjee, R. Selective Molecular Separation by Interfacially Crystallized Covalent Organic Framework Thin Films. *J. Am. Chem. Soc.* **2017**, *139* (37), 13083−13091.
(38) Matsumoto, M.; Valentino, L.; Stiehl, G. M.; Balch, H. B.; Corcos, A. R.; Wang, F.; Ralph, D. C.; Mariñas, B. J.; Dichtel, W. R. Lewis-Acid-Catalyzed Interfacial Polymerization of Covalent Organic Framework Films. *Chem.* **2018**, *4* (2), 308−317.
(39) Sun, B.; Zhu, C.-H.; Liu, Y.; Wang, C.; Wan, L.-J.; Wang, D. Oriented Covalent Organic Framework Film on Graphene for Robust Ambipolar Vertical Organic Field-Effect Transistor. *Chem. Mater.* **2017**, *29* (10), 4367−4374.
(40) Huang, P.; Lethien, C.; Pinaud, S.; Brousse, K.; Laloo, R.; Turq, V.; Respaud, M.; Demortiere, A.; Daffos, B.; Taberna, P. L.; Chaudret, B.; Gogotsi, Y.; Simon, P. On-chip and freestanding elastic carbon films for micro-supercapacitors. *Science* **2016**, *351* (6274), 691−695.
(41) Yang, C.; Schellhammer, K. S.; Ortmann, F.; Sun, S.; Dong, R.; Karakus, M.; Mics, Z.; Loffler, M.; Zhang, F.; Zhuang, X.; Canovas, E.; Cuniberti, G.; Bonn, M.; Feng, X. Coordination Polymer Framework Based On-Chip Micro-Supercapacitors with AC Line-Filtering Performance. *Angew. Chem., Int. Ed.* **2017**, *56* (14), 3920−3924.
(42) Gimenez-Marques, M.; Bellido, E.; Berthelot, T.; Simon-Yarza, T.; Hidalgo, T.; Simon-Vazquez, R.; Gonzalez-Fernandez, A.; Avila, J.; Asensio, M. C.; Gref, R.; Couvreur, P.; Serre, C.; Horcajada, P. GraftFast Surface Engineering to Improve MOF Nanoparticles Furtiveness. *Small* **2018**, *14* (40), 1801900.
(43) Frati, F.; Hunault, M.; de Groot, F. M. F. Oxygen K-edge X-ray Absorption Spectra. *Chem. Rev.* **2020**, *120* (9), 4056−4110.
(44) Wu, S.; Wang, W.; Li, M.; Cao, L.; Lyu, F.; Yang, M.; Wang, Z.; Shi, Y.; Nan, B.; Yu, S.; Sun, Z.; Liu, Y.; Lu, Z. Highly durable organic electrode for sodium-ion batteries via a stabilized α-C radical intermedia. *Nat. Commun.* **2016**, *7*, 13318.
(45) Yang, C.; Dong, R.; Wang, M.; Petkov, P. S.; Zhang, Z.; Wang, M.; Han, P.; Ballabio, M.; Brauninger, S. A.; Liao, Z.; Zhang, J.; Schwotzer, F.; Zschech, E.; Klauss, H. H.; Canovas, E.; Kaskel, S.; Bonn, M.; Zhou, S.; Heine, T.; Feng, X. A semiconducting layered metal-organic framework magnet. *Nat. Commun.* **2019**, *10* (1), 3260.
(46) Jin, S.; Ding, X.; Feng, X.; Supur, M.; Furukawa, K.; Takahashi, S.; Addicoat, M.; El-Khouly, M. E.; Nakamura, T.; Irle, S.; Fukuzumi, S.; Nagai, A.; Jiang, D. Charge dynamics in a donor-acceptor covalent organic framework with periodically ordered bicontinuous heterojunctions. *Angew. Chem., Int. Ed.* **2013**, *52* (7), 2017−2021.
(47) Elbourne, A.; McDonald, S.; Voichovsky, K.; Endres, F.; Warr, G. G.; Atkin, R. Nanostructure of the Ionic Liquid-Graphite Stern Layer. *ACS Nano* **2015**, *9* (7), 7608−7620.
(48) Wang, J.; Polleux, J.; Lim, J.; Dunn, B. Pseudocapacitive Contributions to Electrochemical Energy Storage in TiO2 (Anatase) Nanoparticles. *J. Phys. Chem. C* **2007**, *111* (40), 14925−14931.
(49) Jiang, Y.; Liu, J. Definitions of Pseudocapacitive Materials: A Brief Review. *Energy Environ. Mater.* **2019**, *2* (1), 30−37.
(50) Ardizzone, S.; Fregonara, G.; Trasatti, S. Inner" and "outer" active surface of RuO2 electrodes. *Electrochim. Acta* **1990**, *35* (1), 263−267.
(51) Zhang, L.; Zhang, F.; Yang, X.; Long, G.; Wu, Y.; Zhang, T.; Leng, K.; Huang, Y.; Ma, Y.; Yu, A.; Chen, Y. Porous 3D graphene-based bulk materials with exceptional high surface area and excellent conductivity for supercapacitors. *Sci. Rep.* **2013**, *3*, 1408.
(52) Izadi-Najafabadi, A.; Yasuda, S.; Kobashi, K.; Yamada, T.; Futaba, D. N.; Hatori, H.; Yumura, M.; Iijima, S.; Hata, K. Extracting the full potential of single-walled carbon nanotubes as durable supercapacitor electrodes operable at 4 V with high power and energy density. *Adv. Mater.* **2010**, *22* (35), 235−241.
(53) Zhu, Y.; Murali, S.; Stoller, M. D.; Ganesh, K. J.; Cai, W.; Ferreira, P. J.; Pirkle, A.; Wallace, R. M.; Cychosz, K. A.; Thommes, M.; Su, D.; Stach, E. A.; Ruoff, R. S. Carbon-based supercapacitors produced by activation of graphene. *Science* **2011**, *332* (6037), 1537−1541.